



Hybrid organosilicon/polyol phantom for photoacoustic imaging

FULVIO RATTO, LUCIA CAVIGLI,* CLAUDIA BORRI, SONIA CENTI,
GIADA MAGNI, MARINA MAZZONI, AND ROBERTO PINI

Istituto di Fisica Applicata 'Nello Carrara' IFAC-CNR, Via Madonna del Piano, 10, 50019 Sesto Fiorentino (FI), Italy

*l.cavigli@ifac.cnr.it

Abstract: The rapid development of hardware and software for photoacoustic technologies is urging the establishment of dedicated tools for standardization and performance assessment. In particular, the fabrication of anatomical phantoms for photoacoustic imaging remains an open question, as current solutions have not yet gained unanimous support. Here, we propose that a hybrid material made of a water-in-oil emulsion of glycerol and polydimethylsiloxane may represent a versatile platform to host a broad taxonomy of hydrophobic and hydrophilic dyes and recapitulate the optical and acoustic features of bio tissue. For a full optical parameterization, we refer to Wróbel, *et al.* [Biomed. Opt. Express 7, 2088 (2016)], where this material was first presented for optical imaging. Instead, here, we complete the picture and find that its speed of sound and acoustic attenuation resemble those of pure polydimethylsiloxane, i.e. respectively 1150 ± 30 m/s and 3.5 ± 0.4 dB/(MHz·cm). We demonstrate its use under a commercial B-mode scanner and a home-made A-mode stage for photoacoustic analysis to retrieve the ground-truth encoded in a multilayer architecture containing indocyanine green, plasmonic particles and red blood cells. Finally, we verify the stability of its acoustic, optical and geometric features over a time span of three months.

© 2019 Optical Society of America under the terms of the [OSA Open Access Publishing Agreement](#)

1. Introduction

Anatomical phantoms represent a key asset for the translational development, performance assessment and standardization of new medical imaging technologies [1–3]. In particular, as new technological concepts come to light, there emerge new challenges on the design of artificial materials that may encode the biophysical features and enable an impartial validation of the technical specs of interest. Of course, this issue becomes more complex as the technological platforms are more multimodal, correlative or hybrid or involve multiple scales, anatomical sites or medical problems.

In this context, a prominent case is photoacoustic imaging (PAI) or bimodal PAI / ultrasound imaging, where the mechanism of contrast is optical or both optical and acoustic, and typically allows for spectral resolution; the detection is acoustic; the spatial resolution is optical or acoustic; the scale spans from individual circulating cells to the full body of small animals or the human breast [4]; and the anatomical site is anywhere from the cornea [5] to the breast [6], brain [7, 8], retina [5], skin [9], etc. As such, PAI has been implemented in a wide assortment of complementary setups for microscopy with optical or acoustic resolution [10, 11], tomography or mammoscopy [6, 12], hand-held systems [13], flow cytometry [14–16], thermometry [17], etc. In addition, PAI or bimodal PAI / ultrasound imaging have found application in a broad variety of pathological conditions, including, in particular, cardiovascular disease [18, 19] and cancer [20], where relevant hallmarks include the total concentration of hemoglobin and/or melanin, the oxygen saturation of hemoglobin, the arrangement of blood vessels, or the accumulation of exogenous optical contrast agents, such as organic dyes, plasmonic particles, etc.

The materials implemented to support the rapid technological progress of PAI are several [21]

and include agarose [22] or chitosan [23, 24] hydrogel, freeze-thawed aqueous polyvinyl alcohol (PVA) [25, 26], polyvinyl chloride plastisol (PVCP) [21, 27–30], or gel wax [31], to say a few. However, there is currently no general consensus on a unitary standard for cross-platform implementation, as each solution presents drawbacks that are more or less important in one context or the other. Some materials are rather unstable (agarose, in terms of dehydration, biological contamination and smearing of dyed inserts [21], or gel wax, which softens below 60°C), some entail harsh processing conditions that may be incompatible with (bio)dyes (PVCP) or provide heterogeneous texture (freeze-thawed aqueous PVA [26]), some require the addition of exogenous (micro)scatterers that may suffer from flocculation or sedimentation (PVCP, gel wax [32]), some are incompatible with lipophilic dyes (agarose, chitosan, freeze-thawed aqueous PVA), some with hydrophilic dyes (PVCP, gel wax), and the potential to encode anatomical micro or hierarchical structures remains a general issue.

In a recent paper [33], we contributed to test the use of an ubiquitous elastomer as polydimethylsiloxane (PDMS). PDMS has established as a common platform for phantoms for optical imaging [34], is stable and convenient for fabrication, provides acoustic versatility, in terms of attenuation and speed of sound [35], and is ideal for integration with microfluidic tools [36, 37], which may represent a direct roadmap for the inscription of faithful anatomical features. In particular, we demonstrated the use of PDMS in association to basic microfluidic circuitry to verify the spatial resolution of a commercial B-mode scanner from FUJIFILM VisualSonics Inc, Toronto, ON, Canada, model Vevo LAZR. However, PDMS retains some of the nuisances of previous solutions, requires the addition of exogenous (micro)scatterers and is incompatible with hydrophilic dyes.

More recently, M.S. Wróbel et al [38] proposed a novel material for phantoms for optical imaging made of a water-in-oil emulsion of glycerol droplets in a PDMS continuum. This material displays intrinsic optical scattering, which may span over the entire range of biological tissue with the ratio of glycerol to PDMS and adds little more complexity to the fabrication of PDMS alone. We show that this material practically retains the acoustic features of PDMS and enables the inclusion of hydrophilic dyes as well as more complex pigments, such as plasmonic particles and red blood cells.

2. Materials and methods

2.1. Constituents of phantoms

SYLGARD®184 PDMS kit was purchased from Premier Farnell Ltd, Leeds, UK. All other chemicals were acquired from Merck & Co Inc, Whitehouse Station, NJ, USA, unless otherwise specified. The basic protocol for the fabrication of the phantoms was derived from the prescriptions by M.S. Wróbel et al [38] with minor modifications. In particular, we implemented an intermediate version with a ratio of part A (monomer) : part B (curing agent) : glycerol of 10 : 1 : 4 (w : w : w) by first mixing part A and part B and letting the polymerization begin in a low-vacuum (200 mbar) chamber at 18°C for 6 hrs, then gently incorporating glycerol, letting at rest in the same vacuum chamber for another 18 hrs and then in a stove at 30°C for another 48 hrs. By letting the polymerization begin at 18°C for 6 hrs before the addition of glycerol, we enhanced the viscosity of the mixture, which helped to stabilize and standardize the emulsion. We observed that, after about 18 to 36 hrs in the stove, the emulsion was rather solid but still gluey to the touch, which was exploited to fabricate multilayer architectures without a strong mechanical interface. In any case, samples were used after at least another 72 hrs on the shelf.

In an attempt to challenge the versatility of this protocol, we prepared dyed variants of the same basis by modifying the glycerol component with three cases of hydrophilic or amphiphilic dyes that collectively cover the entire visible to near infrared window, exhibit different nature, and have played a key role in the history of PAI, such as indocyanine green (ICG) [22, 39], gold nanorods (GNRs) [40, 41] and whole red blood cells (RBCs) [10, 15, 16].

1 mg mL⁻¹ ICG in glycerol was mixed and left in the dark for at least 48 hrs. Within the first 24 hrs, we observed a change of the mixture from turbid to apparently clear, as the cyanine dye underwent slow and progressive solvation.

GNRs were synthesized and modified with polyethylene glycol according to the protocols in refs [42, 43]. Thereafter, PEGylated GNRs were transferred into a volatile solvent as methanol, pelleted and mixed with glycerol to a final concentration of 200 $\mu\text{g mL}^{-1}$. This mixture was left in the vacuum chamber for about 12 hrs, until its viscosity recovered from almost as thin as alcohol to that of glycerol, upon evaporation of methanol.

RBCs were collected from the blood of a New Zealand albino rabbit in agreement with Good Laboratory Practice for the use of animals and in accordance with European Union Regulations (Directive 2010/63/EU). Male albino rabbits were kept in individual cages and maintained on a 12/12 hrs light/dark cycle at 22-23°C. Food and water were provided ad libitum. In accordance with Three Rs principles, blood was harvested immediately after death from an animal sacrificed by humane method for another research purpose. Full blood was treated with 0.32% sodium citrate to avoid coagulation [44] and RBCs were separated by centrifugation at 3000 rpm for 20 minutes, fixed in 0.25% glutaraldehyde solution for 10 minutes at 4°C, dehydrated in methanol for 3 minutes at 4°C, pelleted, re-suspended in glycerol to a final concentration double of that of full blood, treated in the vacuum chamber as the suspension of GNRs, and then stored at 4°C for another 24 hrs.

All samples of dyed polyol were brought to room temperature and then mixed with PDMS with the same exact protocol as blank glycerol.

2.2. Phantoms and setup for acoustic characterization

For acoustic characterization, we poured the mixture of PDMS and blank glycerol into a set of home-made aluminum bowls bottomed with an acoustic reflector. The latter was made of an aluminum cylinder cut from a rod of nominal diameter 5 cm into slices of thickness 1 cm $\pm 0.1\%$. In particular, we poured 0, or about 35, 45 or 55 mL of the mixture, which enclosed and progressively buried the aluminum reflector for a depth of about one to several mm.

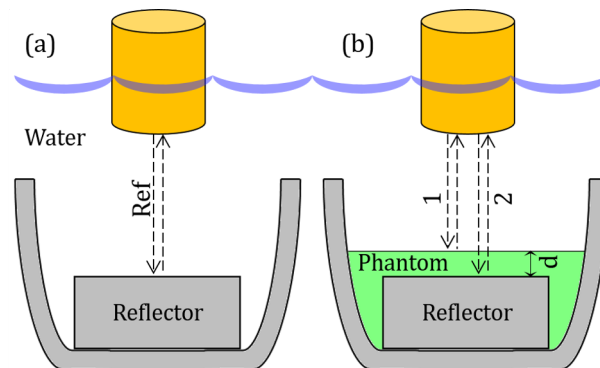


Fig. 1. Sketch of the acoustic set-up, illustrating the use of an empty bowl (a) and a bowl containing a sample (b). Keys are explained in the main text.

The acoustic setup sketched in Fig. 1 was derived from the concept reported in [31] and mounted in a vertical reflection configuration. In brief, the system consisted of a tank filled with DI water, an immersion ultrasound transducer (single element, unfocused, model V311, Olympus Panametrics, Tokyo, Japan) resonating at a center frequency of 10 MHz and driven by an ultrasonic square wave pulser/receiver (model 5077PR, Olympus Panametrics, V = 100 V, repetition rate = 2 kHz) and one of the aluminum bowls containing one sample and sitting at the bottom of the tank.

While the echo received from the empty bowl exhibits a single acoustic transient coming from the interface between water and the aluminum reflector (panel (a) of Fig. 1), those from the other samples feature an earlier signal from the interface between water and the phantom and a later one from the interface between the phantom and the aluminum reflector (panel (b) of Fig. 1). A comparison between the records from the empty bowl and those from any other sample provides multiple information. In particular, if t_{ref} and I_{ref} are delay and intensity of the transient from the empty bowl, t_1 , t_2 and I_2 are delay of the earlier signal and delay and intensity of the later signal from any other sample, and c_w is the speed of sound in water, the thickness of the phantom above the aluminum reflector is $d = c_w(t_{ref} - t_1)/2$, the speed of sound in the phantom is $c_{ph} = 2d/(t_2 - t_1)$, and the attenuation through the phantom relates to $\log_{10}(I_2/I_{ref}) + \varepsilon$, where ε accounts for other sources of dissipation, such as both reflections and scattering at the interface between water and the phantom. Instead, we neglect the low attenuation from DI water [45].

2.3. Phantoms and setup for photoacoustic tests

For the photoacoustic tests, we poured multilayer phantoms into standard 35 mm diameter \times 10 mm height petri dishes. The lowermost layer was a 5.8 g mixture of PDMS and blank glycerol, which formed a flat bed, but for some concave meniscus. After 18 hrs in the stove at 30°C, i.e. about one third of the way, baking was suspended to add an intermediate layer, which consisted of three separate droplets of 40 μ L mixture of PDMS and each of the dyed versions of glycerol, i.e. one droplet contained ICG, one GNRs and one RBCs. We observed that each of these droplets spontaneously spread over about 1 cm of the substrate, corresponding to an average thickness in the order of 500 μ m. After 18 hrs in the stove, baking was suspended once again to cast the uppermost layer, which was another 1.4 g mixture of PDMS and blank glycerol that coated each dyed inclusion and conformed to the underlying bed.

These phantoms were first analyzed in terms of optical extinction in a vertical reflection configuration by the use of a miniature spectrometer from Stellarnet Inc, FL, USA (model EPP2000) by scanning over each dyed inclusion and taking a blank slot in their middle as a reference.

For the photoacoustic tests, we implemented two complementary setups. The first was a commercial B-mode scanner from FUJIFILM VisualSonics Inc, model Vevo LAZR-X, providing tunable narrow-band irradiation from an optical parametric oscillator and high-frequency acoustic detection (40 MHz). The second was a home-made test bench mounted in an upright transmittance configuration equipped with multiple optical sources as well as multiple single-element ultrasonic transducers. In particular, we used a supercontinuum fiber laser platform from NKT Photonics A/S, Birkerød, Denmark (model SuperK COMPACT) for ultra broad-band irradiation (450-2400 nm) and an amplified immersion transducer from Olympus Panametrics (mod V382-SU-F, frequency range 3.5 MHz, focal distance 0.83 inch, 40 dB amplifier mod 5676) as receiver. In both cases, samples were removed from the petri dishes and mounted upside down, so that, in the B-mode scanner, both the irradiation and the detection were from below, i.e. it was the thickest blank bed that faced the probe, whereas, in the home-made test bench, the irradiation was from above and the detection from below. The meniscus formed in the petri dishes was exploited to seat the samples on a film of acoustic gel or water of a thickness around 2 mm.

3. Results and discussion

3.1. Morphology of phantoms

Figure 2 displays a photograph of a phantom prepared for the photoacoustic tests and overlays of confocal fluorescence and bright-field transmission micrographs of smears of the emulsions of PDMS and each of the dyed versions of glycerol acquired with a platform from Leica Microsystems GmbH, Wetzlar, Germany, model SP8. Panel (a) gives an idea of the milky

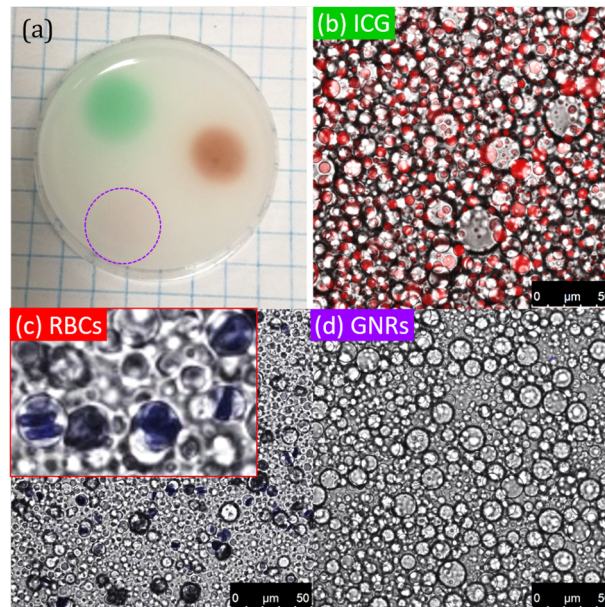


Fig. 2. (a): photograph of a multilayered phantom used for the photoacoustic tests, where the buried inclusions containing ICG, GNRs and RBCs are respectively visible as a green, faint carnation pink and red spot. The location of the GNRs is marked with a violet circle. The side of the squares measures 5 mm. (b) to (d): overlays of confocal fluorescence and bright-field transmission micrographs of smears of samples containing the designated dyes. Scale bars are 50 μm . The inset in (c) is magnified four times, in order to display the individual cells and their stacks. All images were acquired on day 3 post-synthesis.

appearance of the phantoms, which exhibit a uniform slight grayish coloration consistent with the spectra of optical absorbance and scattering reported by M.S. Wróbel et al [38] and let one distinguish the dyed inclusions below a skin of a depth around 1.5 mm as a green spot for ICG, a faint carnation pink one for the GNRs and a red one for the RBCs.

Panels (b) to (d) of Fig. 2 collectively corroborate the assumption of a water-in-oil emulsion of glycerol droplets in a PDMS continuum. However, we observed some tendency of the phantoms to deform when left to soak in water for several hrs, as under the effect of some osmotic pressure. This occurrence may point to some degree of interconnectivity of the glycerol pores or some permeability of the PDMS backbone, which may allow for some (inter)exchange of water and glycerol. Whether its incidence may be reproducible and/or prove to be profitable for the fabrication of a new generation of porous phantoms will be the subject of future investigation. Here, we note that the paper by M.S. Wróbel et al [38] suggested the use of this material as a testbed for optical clearing [46], probably implying the vision to replace the glycerol component with another agent. The fluorescence from ICG and hemoglobin demonstrate their localization within the glycerol phase seen as a constellation of spherical droplets. Unfortunately, the weak fluorescence of the GNRs does not allow for their visualization. Besides, PEGylated GNRs may be quantitatively partitioned between both components, by virtue of their amphiphilic profile. The close-up in panel (c) also reveals that the RBCs maintained their distinctive morphology as well as their natural tendency to pile up in rouleaux.

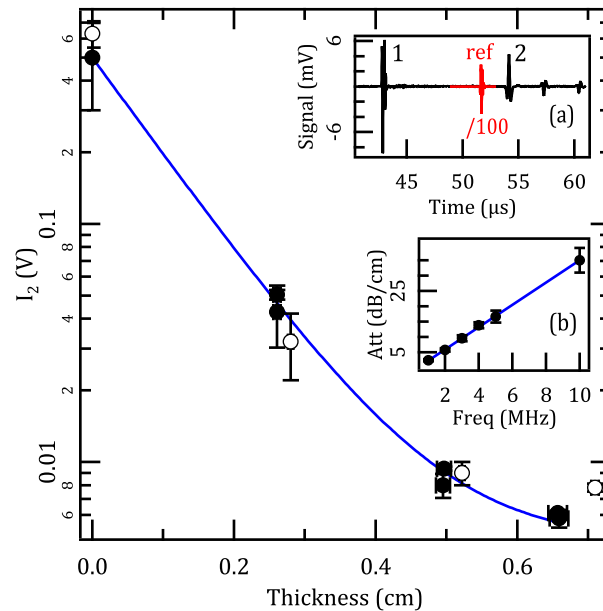


Fig. 3. Intensity of the reflection from the interface between water or the sample and the aluminum reflector vs thickness of the sample. Full symbols refer to a set of measurements performed on day 3 post-synthesis and were fitted to an exponential decay. Empty symbols were acquired on day 90 post-synthesis. Inset (a): reference echo from an empty bowl (red line, divided by hundred) and that from a bowl containing a sample and featuring two principal transients (black line), see Fig. 1. Inset (b): compilation of different values for the attenuation coefficient vs frequency of the acoustic signal. The data points until a frequency of 5 MHz are derived from [35] and refer to blank PDMS. The data point at 10 MHz originates from the exponential fit displayed in the main panel for an emulsion of PDMS and glycerol on day 3 post-synthesis. Our value is a good linear extrapolation of those from blank PDMS ($R^2 = 0.9994$).

3.2. Acoustic parameters of phantoms

The upper inset in Fig. 3 confirms that a comparison between the echo recorded from the empty bowl and those from any other sample displays significant differences. Apart from the occurrence of two rather than a unique reflection, as we have already anticipated under Section 2, we note that the presence of the phantom scales down the amplitude of both transients by a factor around 100. The reason why the earlier signal is weak is that the impedance mismatch between water and the phantom is low, which is desirable. The later signal is rather low as well, mainly due to the effect of attenuation across the phantom and partly also to both reflections and scattering at the former interface. Another difference is that the reflection from the aluminum reflector is delayed in the presence of the phantom, because its speed of sound is lower than that of water.

As we have already explained in Section 2, each acoustic record allows for an independent measurement of the speed of sound in the phantom. We took 5 data points around the center of each phantom in two separate sessions, for a total of 30 samplings. The average is $c_{ph} = 1150 \pm 30$ m/s, or about 22 % slower than the ref value of $c_w = 1482$ m/s [47] at 20°C. Our value is only about 8 % higher than that of pure PDMS [35] and far from that of glycerol around 1920 m/s, which may convey a slight favorable correction. In any case, we note that pure PDMS has already found application both as an acoustic [35] and photoacoustic [33] testbed and holds the potential for a fine modulation with relevant parameters, such as the composition of the two-phase mixture

or the use of additives [35]. We conjecture that the implementation of those modifications in our elastomer may convey similar results, because it is the PDMS backbone that mostly determines the speed of sound in our emulsion.

Figure 3 also displays a plot of the relative attenuation of the signal from the aluminum reflector vs. the thickness of the various phantoms. The overall profile follows an exponential decay with an offset that we mostly ascribe to the reflections and residual scattering at the boundary between water and the phantom. From our plot, we estimate an attenuation coefficient $\alpha_{ph} = 3.5 \pm 0.4$ dB/(MHz·cm), which is close to that of tendon, i.e. 4.7 dB/(MHz·cm) [3]. Also in this case, we conjecture that the modification of the PDMS component may enable the simulation of other cases of bio tissue, such as cortical and trabecular bone, connective tissue and muscle [3]. For instance, Cafarelli et al [35] achieved tunability over a factor of 3.5 by lowering the concentration of the curing agent or adding ceramic particles. Inset (b) demonstrates that our value extrapolates well the data reported by Cafarelli et al [35] for pure PDMS with the same composition of monomer and curing agent, which justifies our speculation.

3.3. Photoacoustic tests

Panel (a) of Fig. 4 displays the spectra of optical extinction retrieved from different locations of the phantoms used for the photoacoustic tests, viz. above the inclusions containing ICG, GNRs and RBCs. The principal band of ICG resembles that found in plasma for a concentration above about $500 \mu\text{g mL}^{-1}$ [48] or in hybrid formulations [49]. The plasmonic band of the GNRs is rather broad, probably due to an interplay of some aggregation [50] in glycerol and partial transfer [51] to PDMS. The spectrum from the RBCs is rather consistent with that of deoxygenated hemoglobin [8], as may result from the antioxidant activity of glycerol, the treatment in the vacuum chamber and the low permeability of PDMS to oxygen [52]. Altogether, these observations suggest some advantages and disadvantages of our phantoms. Disadvantages include the need for a higher local concentration of the hydrophilic dye, i.e. by a factor 15/4, to achieve a certain global target, or the limited versatility of glycerol as a protic solvent. Advantages include the protection of the hydrophilic payload against the external environment, as may result from the confinement exerted by the PDMS scaffold and enable new perspectives, such as the fabrication of hemoglobin inclusions retaining a certain level of oxygenation, in order to encode arterial and venous vessels [30], hypoxic lesions, etc.

In order to illustrate the application of our phantoms in the broad context of PAI, we performed a set of preliminary controls. The micrographs in panel (d) of Fig. 4 show representative B-scans taken with the Vevo LAZR-X operated at different wavelength, i.e 690, 750 and 900 nm. The inclusions containing ICG and RBCs are well visible as thin lenslets of high photoacoustic intensity and their contrast scales with the appropriate wavelength. Also their spectra of optical absorbance reconstructed by the Vevo LAZR-X recapitulate reasonably well those measured with the miniature spectrometer (data not shown). However, we did not quite succeed to image the inclusion containing the GNRs, probably due to their photoinstability above a damage threshold of 5 to 10 mJ cm^{-2} [23, 24], which is at least an order of magnitude below the optical fluence delivered by the Vevo LAZR-X (more than 150 mJ cm^{-2}). When we turned the samples face-up again, we found a deep pink color, which is an explicit clue to an irreversible deformation of the GNRs to gold nanospheres [53]. We suggest that the analysis of the photophysical parameters of optical contrast agents may be another field of application for our phantoms.

Finally, our A-scans acquired with a supercontinuum source of irradiation reveal a composite profile that accounts for the weaker absorbance from PDMS [38] and the stronger response from the dyed inclusions. Light from the supercontinuum fiber laser was weakly focused with an achromatic lens to a spot of a diameter of $300 \mu\text{m}$ on the sample, in order to give an optical fluence of 6 mJ cm^{-2} over a broad band from about 450 to 2400 nm. The acoustic transducer was focused to a depth roughly corresponding to that of the dyed inclusions. Results are shown in Fig.

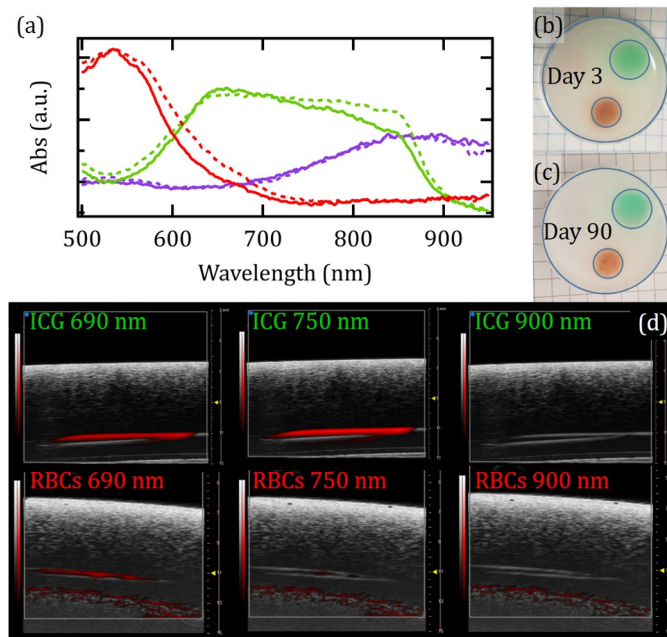


Fig. 4. (a): spectra of optical extinction from different locations of a multilayered phantom. The solid lines refer to a set of measurements performed on day 3 post-synthesis. The broken lines were acquired on day 90 post-synthesis. (b) and (c): photographs of the same multilayered phantom taken at days 3 and 90 post-synthesis, respectively, and superimposed with fiducial circles of the same size and location. The side of the squares measures 5 mm. (d): multimodal photoacoustic / ultrasound sections acquired at day 7 post-synthesis with a Vevo LAZR-X over the locations corresponding to the buried inclusions containing ICG or RBCs at different wavelength, i.e 690, 750 or 900 nm. Each field of view measures about $10 \text{ mm} \times 8 \text{ mm}$. The photoacoustic signal is encoded in red and the ultrasound echo in white. For the photoacoustic channel, the gain was adjusted in order to optimize the contrast in each panel. Note that ICG is visible at 690 and 750 nm, but rather not at 900 nm, and the RBCs are discernible at 690 nm and already nearly disappear at 750 nm and beyond. The lower feature in the photoacoustic maps corresponding to the RBCs relates to the interface between the blank overlay with its crescent shape and the underlying gel film.

5. The principal features in our A-scans are a stronger transient around $15 \mu\text{s}$ that originates from the dyed inclusions and scales with their integrated optical density, and a weaker signal around $17 \mu\text{s}$ that corresponds to the blank overlay distal from the acoustic transducer. Additional features include multiple reflections at later delay, whereas any earlier signal from the blank bed is dampened by the effect of optical scattering. In this case, the optical fluence was much lower than the damage threshold of the GNRs, because each individual particle in the heterogeneous mixture was in resonance with a small percent of the ultra broad-band excitation [23]. The overall data qualitatively corroborates the ground-truth encoded in the phantoms and suggests substantial possibilities for translational developments.

3.4. Stability over time

We repeated the analysis of the acoustic and optical parameters of our phantoms 90 days after fabrication, with the intent to challenge their medium-term stability. All samples were stored on the shelf in air. Figure 3 (empty symbols) reveals that, on average, the thickness of the samples swelled by 5 %, which we ascribe to some adsorption of water from environmental moisture. The

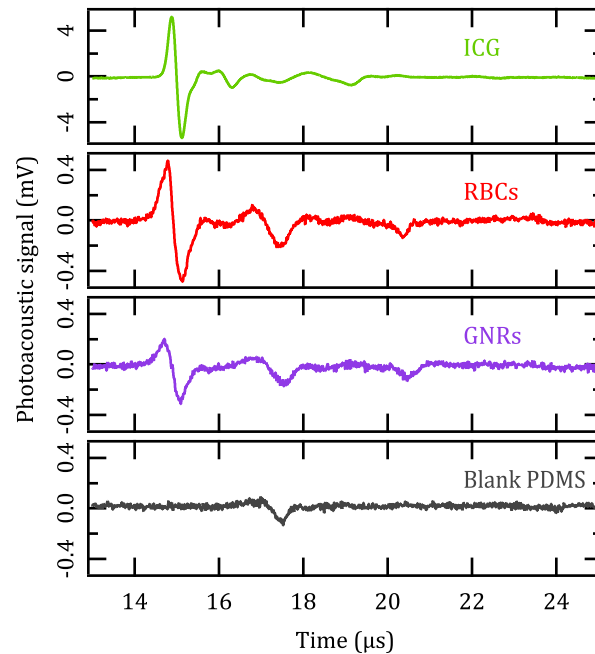


Fig. 5. Representative excerpts of raw photoacoustic A-scans from the designated locations of a multilayered phantom acquired on day 9 post-synthesis.

speed of sound increased from 1150 ± 30 to 1190 ± 30 m/s whereas the attenuation coefficient decreased from 3.5 ± 0.4 to 3.3 ± 0.4 dB/(MHz·cm). Therefore, the acoustic parameters remained consistent over time. Panel A of Fig. 4 reveals that the spectra of optical extinction from the various inclusions underwent subtle variations pointing to a consolidation of the oxygen desaturation of hemoglobin [8] and an enhancement of the solvation of ICG [48]. The former is rather surprising for a sample kept in air and confirms the antioxidant activity of glycerol and the sealing effect of PDMS. The latter is consistent with our initial observation that the dissolution of ICG in glycerol is a relatively slow process. Instead, no modification was detected for the inclusion containing GNRs. Panels (b) and (c) of Fig. 4 show that all variations were hardly discernible to the naked eye. In particular, the lateral size of the dyed inclusions underwent no visible smearing, which points to a negligible diffusivity of ICG and the RBCs from glycerol droplet to droplet. Taken together, our phantoms display a shelf-life exceeding three months, which may be adequate for most practical applications in PAI.

4. Conclusions

In conclusion, we propose that the material developed by M.S. Wróbel et al [38] and made of a water-in-oil emulsion of glycerol droplets in a PDMS continuum may host hydrophilic dyes and serve as a convenient platform for standardization in PAI. We have tested the inclusion of a diversified taxonomy of hydrophilic dyes into the glycerol component, i.e. ICG, GNRs and RBCs. We have shown that the acoustic properties of the final composite derive from those of pure PDMS, i.e. a speed of sound around 1150 ± 30 m/s and an attenuation around 3.5 ± 0.4 dB/(MHz·cm), which resembles the value of tendon and may undergo substantial modulation to approach other cases of representative bio tissue. We have verified the use of this material under a commercial B-mode scanner and a home-made A-mode stage for photoacoustic analysis to

recapitulate the ground-truth encoded in a multilayer architecture. Finally, we have addressed its shelf-life and found that its acoustic and optical parameters remain consistent over at least three months. Overall, we believe that a water-in-oil emulsion featuring a PDMS backbone may represent a versatile and biomimetic strategy for the fabrication of phantoms for PAI or hybrid PAI / ultrasound imaging, which may enable an immediate integration of microfluidic tools to simulate such structures as arterial and venous vessels. In the future, we will explore different directions, such as the optimization of the manufacturing throughput time and tunability of the acoustic parameters with the processing conditions as the curing temperature or the modification of the PDMS component, i.e. the composition of the two-phase mixture, the use of additives [35], etc. In addition, we will consider the replacement of the polyol component with other viscous or complex solvents, such as gelatin or other polymeric pastes. We are confident that our contribution will inspire more work to bring new materials and manufacturing technologies to fruition in the field of photoacoustic standardization.

Funding

ERA-NET Cofund Transnational Call "PhotonicSensing" - H2020 under grant agreement No. 688735 Project: "PLABAN, Advanced Plasmonic Biosensor Analysis of Nucleic Acid Biomarker"; Joint Research Project CNR (Italy) / RFBR (Russia) HYPNOSIs; AIRC- ENTE CRF Project: INPACT.

Acknowledgments

The authors wish to acknowledge Prof. Annarosa Arcangeli and Dr Tiziano Lottini (Department of Experimental and Clinical Medicine, University of Florence) for their support on the experiments with the Vevo LAZR-X, the group of Prof. Emanuela Masini (Department NEUROFARBA, University of Florence) for providing the blood sample, and the International Photoacoustic Standardisation Consortium (IPASC) for fruitful discussions.

Disclosures

The authors declare that there are no conflicts of interest related to this article.

References

1. R. Cubeddu, A. Pifferi, P. Taroni, A. Torricelli, and G. Valentini, "A solid tissue phantom for photon migration studies," *Phys. Medicine Biol.* **42**, 1971–1979 (1997).
2. B. W. Pogue and M. S. Patterson, "Review of tissue simulating phantoms for optical spectroscopy, imaging and dosimetry," *J. Biomed. Opt.* **11**, 041102 (2006).
3. M. O. Culjat, D. Goldenberg, P. Tewari, and R. S. Singh, "A review of tissue substitutes for ultrasound imaging," *Ultrasound Med Biol* **36**, 861 – 873 (2010).
4. L. V. Wang and S. Hu, "Photoacoustic tomography: In vivo imaging from organelles to organs," *Science* **335**, 1458–1462 (2012).
5. W. Liu and H. F. Zhang, "Photoacoustic imaging of the eye: A mini review," *Photoacoustics* **4**, 112 – 123 (2016). Special Issue: Photoacoustic Microscopy.
6. M. Heijblom, D. Piras, F. M. van den Engh, M. van der Schaaf, J. M. Klaase, W. Steenbergen, and S. Manohar, "The state of the art in breast imaging using the twente photoacoustic mammoscope: results from 31 measurements on malignancies," *Eur. Radiol.* **26**, 3874–3887 (2016).
7. X. Wang, Y. Pang, G. Ku, X. Xie, G. Stoica, and L. V. Wang, "Noninvasive laser-induced photoacoustic tomography for structural and functional in vivo imaging of the brain," *Nat. Biotechnol.* **21**, 803–806 (2003).
8. X. Wang, X. Xie, G. Ku, L. V. Wang, and G. Stoica, "Noninvasive imaging of hemoglobin concentration and oxygenation in the rat brain using high-resolution photoacoustic tomography," *J. Biomed. Opt.* **11**, 024015 (2006).
9. K. S. Valluru, K. E. Wilson, and J. K. Willmann, "Photoacoustic imaging in oncology: Translational preclinical and early clinical experience," *Radiology* **280**, 332–349 (2016).
10. C. Zhang, K. Maslov, and L. V. Wang, "Subwavelength-resolution label-free photoacoustic microscopy of optical absorption in vivo," *Opt. Lett.* **35**, 3195–3197 (2010).
11. J. Yao and L. V. Wang, "Photoacoustic microscopy," *Laser & Photonics Rev.* **7**, 758–778 (2013).

12. A. Oraevsky, R. Su, H. Nguyen, J. Moore, Y. Lou, S. Bhadra, L. Forte, M. Anastasio, and W. Yang, "Full-view 3d imaging system for functional and anatomical screening of the breast," *Proc.SPIE* **10494**, 104942Y (2018).
13. M. W. Schellenberg and H. K. Hunt, "Hand-held optoacoustic imaging: A review," *Photoacoustics* **11**, 14 – 27 (2018).
14. V. V. Tuchin, A. Tárnok, and V. P. Zharov, "In vivo flow cytometry: A horizon of opportunities," *Cytom. Part A* **79A**, 737–745 (2011).
15. E. I. Galanzha and V. P. Zharov, "Photoacoustic flow cytometry," *Methods* **57**, 280 – 296 (2012).
16. V. Gnyawali, E. M. Stroh, J.-Z. Wang, S. S. H. Tsai, and M. C. Kolios, "Simultaneous acoustic and photoacoustic microfluidic flow cytometry for label-free analysis," *Sci. Reports* **9**, 1585 (2019).
17. J. Yao, H. Ke, S. Tai, Y. Zhou, and L. V. Wang, "Absolute photoacoustic thermometry in deep tissue," *Opt. Lett.* **38**, 5228–5231 (2013).
18. B. Wang, E. Yantsen, T. Larson, A. B. Karpouk, S. Sethuraman, J. L. Su, K. Sokolov, and S. Y. Emelianov, "Plasmonic intravascular photoacoustic imaging for detection of macrophages in atherosclerotic plaques," *Nano Lett.* **9**, 2212–2217 (2009).
19. K. Jansen, A. F. W. van der Steen, H. M. M. van Beusekom, J. W. Oosterhuis, and G. van Soest, "Intravascular photoacoustic imaging of human coronary atherosclerosis," *Opt. Lett.* **36**, 597–599 (2011).
20. S. Mallidi, G. P. Luke, and S. Emelianov, "Photoacoustic imaging in cancer detection, diagnosis, and treatment guidance," *Trends Biotechnol.* **29**, 213 – 221 (2011).
21. M. Fonseca, B. Zeqiri, P. C. Beard, and B. T. Cox, "Characterisation of a phantom for multiwavelength quantitative photoacoustic imaging," *Phys. Medicine Biol.* **61**, 4950–4973 (2016).
22. Y.-W. Wang, Y.-Y. Fu, Q. Peng, S.-S. Guo, G. Liu, J. Li, H.-H. Yang, and G.-N. Chen, "Dye-enhanced graphene oxide for photothermal therapy and photoacoustic imaging," *J. Mater. Chem. B* **1**, 5762–5767 (2013).
23. L. Cavigli, M. de Angelis, F. Ratto, P. Matteini, F. Rossi, S. Centi, F. Fusi, and R. Pini, "Size affects the stability of the photoacoustic conversion of gold nanorods," *The J. Phys. Chem. C* **118**, 16140–16146 (2014).
24. L. Cavigli, A. Cini, S. Centi, C. Borri, S. Lai, F. Ratto, M. de Angelis, and R. Pini, "Photostability of gold nanorods upon endosomal confinement in cultured cells," *The J. Phys. Chem. C* **121**, 6393–6400 (2017).
25. A. Kharine, S. Manohar, R. Seeton, R. G. M. Kolkman, R. A. Bolt, W. Steenbergen, and F. F. M. de Mul, "Poly(vinyl alcohol) gels for use as tissue phantoms in photoacoustic mammography," *Phys. Medicine Biol.* **48**, 357–370 (2003).
26. W. Xia, D. Piras, M. Heijblom, W. Steenbergen, T. G. van Leeuwen, and S. Manohar, "Poly(vinyl alcohol) gels as photoacoustic breast phantoms revisited," *J. Biomed. Opt.* **16**, 16 – 16 – 11 (2011).
27. G. M. Spirou, A. A. Oraevsky, I. A. Vitkin, and W. M. Whelan, "Optical and acoustic properties at 1064 nm of polyvinyl chloride-plastisol for use as a tissue phantom in biomedical optoacoustics," *Phys. Medicine Biol.* **50**, N141–N153 (2005).
28. S. E. Bohndiek, S. Bodapati, D. Van De Sompel, S.-R. Kothapalli, and S. S. Gambhir, "Development and application of stable phantoms for the evaluation of photoacoustic imaging instruments," *PLOS ONE* **8** (2013).
29. W. C. Vogt, C. Jia, K. A. Wear, B. S. Garra, and T. J. Pfeifer, "Biologically relevant photoacoustic imaging phantoms with tunable optical and acoustic properties," *J. Biomed. Opt.* **21**, 21 – 21 – 11 (2016).
30. A. Oraevsky, B. Clingman, J. Zalev, A. Stavros, W. Yang, and J. Parikh, "Clinical optoacoustic imaging combined with ultrasound for coregistered functional and anatomical mapping of breast tumors," *Photoacoustics* **12**, 30 – 45 (2018).
31. E. Maneas, W. Xia, O. Ogunlade, M. Fonseca, D. I. Nikitichev, A. L. David, S. J. West, S. Ourselin, J. C. Hebden, T. Vercauteren, and A. E. Desjardins, "Gel wax-based tissue-mimicking phantoms for multispectral photoacoustic imaging," *Biomed. Opt. Express* **9**, 1151–1163 (2018).
32. C. J. M. Jones and P. R. T. Munro, "Stability of gel wax based optical scattering phantoms," *Biomed. Opt. Express* **9**, 3495–3502 (2018).
33. C. Avigo, N. Di Lascio, P. Armanetti, C. Kusmic, L. Cavigli, F. Ratto, S. Meucci, C. Masciullo, M. Cecchini, R. Pini, F. Fata, and L. Menichetti, "Organosilicon phantom for photoacoustic imaging," *J. Biomed. Opt.* **20**, 20 – 20 – 7 (2015).
34. F. Ayers, A. Grant, D. Kuo, D. J. Cuccia, and A. J. Durkin, "Fabrication and characterization of silicone-based tissue phantoms with tunable optical properties in the visible and near infrared domain," *Proc.SPIE* **6870**, 687007 (2008).
35. A. Cafarelli, A. Verbeni, A. Poliziani, P. Dario, A. Menciassi, and L. Ricotti, "Tuning acoustic and mechanical properties of materials for ultrasound phantoms and smart substrates for cell cultures," *Acta Biomater.* **49**, 368 – 378 (2017).
36. C. M. B. Ho, S. H. Ng, K. H. H. Li, and Y.-J. Yoon, "3d printed microfluidics for biological applications," *Lab Chip* **15**, 3627–3637 (2015).
37. A. K. Au, W. Huynh, L. F. Horowitz, and A. Folch, "3d-printed microfluidics," *Angewandte Chemie Int. Ed.* **55**, 3862–3881 (2016).
38. M. S. Wróbel, A. P. Popov, A. V. Bykov, V. V. Tuchin, and M. Jedrzejewska-Szczerska, "Nanoparticle-free tissue-mimicking phantoms with intrinsic scattering," *Biomed. Opt. Express* **7**, 2088–2094 (2016).
39. G. Ku and L. V. Wang, "Deeply penetrating photoacoustic tomography in biological tissues enhanced with an optical contrast agent," *Opt. Lett.* **30**, 507–509 (2005).
40. A. Agarwal, S. W. Huang, M. O'Donnell, K. C. Day, M. Day, N. Kotov, and S. Ashkenazi, "Targeted gold nanorod contrast agent for prostate cancer detection by photoacoustic imaging," *J. Appl. Phys.* **102**, 064701 (2007).

41. F. Ratto, S. Centi, C. Avigo, C. Borri, F. Tatini, L. Cavigli, C. Kusmic, B. Lelli, S. Lai, S. Colagrande, F. Faita, L. Menichetti, and R. Pini, "A robust design for cellular vehicles of gold nanorods for multimodal imaging," *Adv. Funct. Mater.* **26**, 7178–7185 (2016).
42. F. Ratto, P. Matteini, F. Rossi, and R. Pini, "Size and shape control in the overgrowth of gold nanorods," *J. Nanoparticle Res.* **12**, 2029–2036 (2010).
43. F. Tatini, I. Landini, F. Scaletti, L. Massai, S. Centi, F. Ratto, S. Nobili, G. Romano, F. Fusi, L. Messori, E. Mini, and R. Pini, "Size dependent biological profiles of pegylated gold nanorods," *J. Mater. Chem. B* **2**, 6072–6080 (2014).
44. D. M. Adcock, D. C. Kressin, and R. A. Marlar, "Effect of 3.2% vs 3.8% sodium citrate concentration on routine coagulation testing," *Am. J. Clin. Pathol.* **107**, 105–110 (1997).
45. R. Martinez, L. Leija, and A. Vera, "Ultrasonic attenuation in pure water: Comparison between through-transmission and pulse-echo techniques," in *2010 Pan American Health Care Exchanges*, (2010), pp. 81–84.
46. D. Zhu, K. V. Larin, Q. Luo, and V. V. Tuchin, "Recent progress in tissue optical clearing," *Laser & Photonics Rev.* **7**, 732–757 (2013).
47. N. Bilaniuk and G. S. K. Wong, "Speed of sound in pure water as a function of temperature," *J. Acoust. Soc. Am.* **93**, 1609–1612 (1993).
48. M. L. Landsman, G. Kwant, G. A. Mook, and W. G. Zijlstra, "Light-absorbing properties, stability, and spectral stabilization of indocyanine green," *J. Appl. Physiol.* **40**, 575–583 (1976).
49. S. Wang, G. M. Hüttmann, F. Rudnitzki, H. Diddens-Tschoeke, Z. Zhang, and R. Rahmzadeh, "Indocyanine green as effective antibody conjugate for intracellular molecular targeted photodynamic therapy," *J. Biomed. Opt.* **21**, 21 – 21 – 8 (2016).
50. M. Mazzoni, F. Ratto, C. Fortunato, S. Centi, F. Tatini, and R. Pini, "Partial decoupling in aggregates of silanized gold nanorods," *The J. Phys. Chem. C* **118**, 20018–20025 (2014).
51. M. Liu, W.-C. Law, A. Kopwitthaya, X. Liu, M. T. Swihart, and P. N. Prasad, "Exploring the amphiphilicity of pegylated gold nanorods: mechanical phase transfer and self-assembly," *Chem. Commun.* **49**, 9350–9352 (2013).
52. A. Lamberti, S. L. Marasso, and M. Cocuzza, "Pdms membranes with tunable gas permeability for microfluidic applications," *RSC Adv.* **4**, 61415–61419 (2014).
53. R. Mercatelli, F. Ratto, S. Centi, S. Soria, G. Romano, P. Matteini, F. Quercioli, R. Pini, and F. Fusi, "Quantitative readout of optically encoded gold nanorods using an ordinary dark-field microscope," *Nanoscale* **5**, 9645–9650 (2013).